MAGNETOHYDRODYNAMICS Vol. 45 (2009), No. 2, pp. 135–143

LIQUID METAL EXPERIMENTS ON THE HELICAL MAGNETOROTATIONAL INSTABILITY

F. Stefani[1], *G. Gerbeth*[1], *Th. Gundrum*[1],
J. Szklarski[2], *G. Rüdiger*[3], *R. Hollerbach*[4]

[1] *Forschungszentrum Dresden-Rossendorf,*
P.O. Box 510119, D-01314 Dresden, Germany
[2] *Institute of Fundamental Technological Research,*
21 Świętokrzyska, 00-049 Warsaw, Poland
[3] *Astrophysikalisches Institut Potsdam,*
An der Sternwarte 16, D-14482 Potsdam, Germany
[4] *Department of Applied Mathematics, University of Leeds, Leeds, LS2 9JT, UK*

The magnetorotational instability (MRI) plays an essential role in the formation of stars and black holes. By destabilizing hydrodynamically stable Keplerian flows, the MRI triggers turbulence and enables outward transport of angular momentum in accretion discs. We present the results of a liquid metal Taylor–Couette experiment under the influence of helical magnetic fields that show typical features of MRI at Reynolds numbers of the order 1000 and Hartmann numbers of the order 10. Particular focus is laid on an improved experiment, in which split end caps are used to minimize the Ekman pumping.

1. Introduction. Magnetic fields play a double role in the cosmos: first, planetary, stellar, and galactic fields are produced by the homogeneous dynamo effect in moving electrically conducting fluids, second, magnetic fields can accelerate tremendously the formation of stars and black holes by enabling outward directed transport of angular momentum in accretion disks by virtue of the so-called magnetorotational instability (MRI). This instability was discovered as early as 1959, when Velikhov showed that a Taylor-Couette flow in its hydrodynamically stable regime (i.e., with outward increasing angular momentum) can be destabilized by an applied axial magnetic field [1]. It was only in 1991, however, that the importance of MRI for accretion disks in the vicinity of young stars and black holes was realized in a seminal paper by Balbus and Hawley [2].

The last decades have seen tremendous theoretical and computational progress in understanding the dynamo effect and the MRI. The hydromagnetic dynamo effect has even been verified experimentally in large-scale liquid sodium facilities in Riga, Karlsruhe, and Cadarache, and is presently studied in laboratories around the world [3, 4]. In contrast, attempts to study the MRI in the laboratory have been less successful so far. Recently, an MRI-like instability has been observed on the background of a turbulent spherical Couette flow [5], but the original idea that MRI would destabilize a hydrodynamically stable flow was not realized in this experiment. Another interesting MRI-experiment, using a rather short Taylor-Couette-cell, is pursued at Princeton University [6, 7].

One of the basic problems for the experimental investigation of the "standard MRI", with only an axial magnetic field being externally applied, is the need for flows with large magnetic Reynolds number Rm. The crucial point is that the azimuthal field, which is essential for the MRI mechanism to work, must be produced from the applied axial field by induction effects proportional to Rm. The natural question, why not substitute the induction process by externally applying

the azimuthal field as well, was addressed by Hollerbach and Rüdiger [8]. Exemplified in a Taylor–Couette configuration, it was shown that the scaling properties for this "helical MRI", as we call it now, are completely different from those of the "standard MRI". While the latter is governed by the magnetic Reynolds number Rm and the Lundquist number S, the former depends only on the hydrodynamic Reynolds number Re and the Hartmann number Ha. For liquid metals, with their small magnetic Prandtl number Pm, this makes a dramatic difference for the feasibility of MRI experiments, since $\mathrm{Rm} = \mathrm{PmRe}$ and $\mathrm{S} = \mathrm{Pm}^{1/2}\mathrm{Ha}$.

We have to point out, though, that there is no real breach between "standard MRI" and "helical MRI". This can be clearly seen in Fig. 1 of [8], where the critical Rm is plotted against the rotation ratio $\mu := f_\mathrm{o}/f_\mathrm{i}$ of outer to inner cylinder of a Taylor–Couette set-up. The extremely steep increase of this curve at the Rayleigh line, which occurs for a purely axial magnetic field, is just smeared out when an azimuthal field is added. In this paper, we summarize the main results of a first experimental verification of this idea obtained in the framework of the PROMISE experiment (Potsdam ROssendorf Magnetic InStability Experiment), which were already published in [9–12], and we report some new results of an improved version of this experiment.

2. The experimental facility. The basic part of PROMISE is a cylindrical containment vessel V made of copper (see Fig. 1). The inner wall of the vessel V is 10 mm thick, and extends in radius from 22 to 32 mm; the outer wall is 15 mm thick, extending from 80 to 95 mm. This vessel is filled with the eutectic alloy $\mathrm{Ga}^{67}\mathrm{In}^{20.5}\mathrm{Sn}^{12.5}$, which is liquid at room temperatures and whose physical

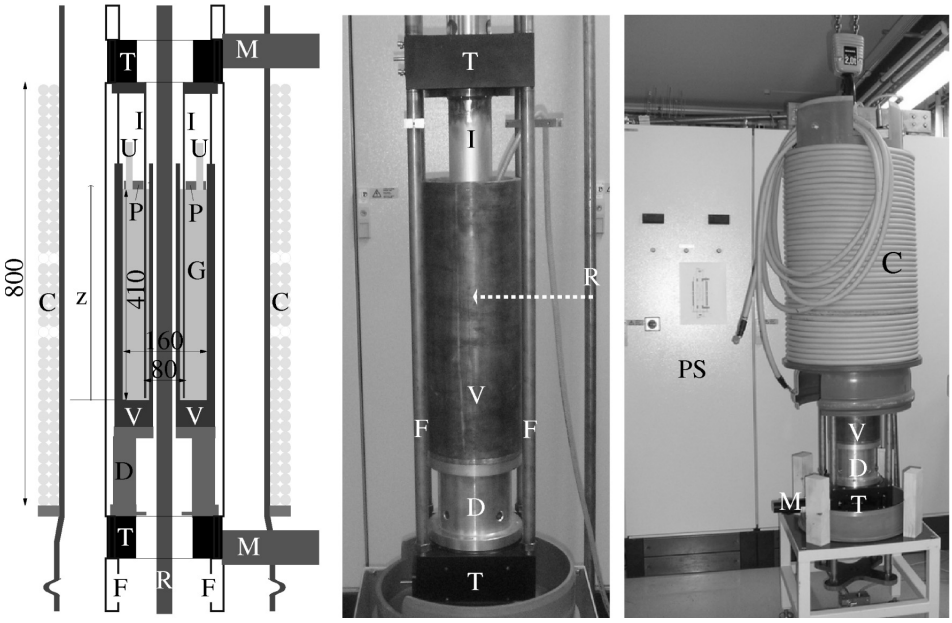

(a) (b) (c)

Fig. 1. The PROMISE experiment. (*a*) Sketch. (*b*) Photograph of the central part. (*c*) Total view with the coil being installed. V – copper vessel, I – inner cylinder, G – GaInSn, U – two ultrasonic transducers, P – plexiglas lid, T – high precision turn-tables, D – aluminum spacer, M – motors, F – frame, C – coil, R – copper rod, PS – power supply for currents up to 8000 A. The indicated dimensions are in mm.

properties at 25°C are as follows: density $\rho = 6.36 \times 10^3$ kg/m^3, kinematic viscosity $\nu = 3.40 \times 10^{-7}$ m^2/s, electric conductivity $\sigma = 3.27 \times 10^6$ $(\Omega\mathrm{m})^{-1}$. The magnetic Prandtl number is then $\mathrm{Pm} = \mu_0 \sigma \nu = 1.40 \times 10^{-6}$. The vessel V, which is completely made of copper in the first version of the experiment (henceforth called PROMISE 1), is fixed, via an aluminum spacer D, on a precision turntable T; the outer copper cylinder of the vessel represents the outer cylinder of the Taylor-Couette cell. The inner copper cylinder I of the Taylor–Couette flow is fixed to an upper turntable, and is immersed into the liquid metal from above. It has a thickness of 4 mm, extending in radius from 36 to 40 mm, thus leaving a gap of 4 mm between this immersed cylinder I and the inner wall of the containment vessel V. The actual Taylor–Couette cell extends in the radial direction over a cylindrical gap of width $d = r_\mathrm{o} - r_\mathrm{i} = 40$ mm, and in the axial direction over the liquid metal height $h = 400$ mm, resulting in an aspect ratio of 10.

In the PROMISE 1 configuration, the upper endplate is a non-rotating Plexiglass lid P fixed to the frame F. The bottom, however, is simply part of the copper vessel V, and rotates with the outer cylinder. With respect to both their rotation rates and electric conductivities, there is thus a clear asymmetry in the end caps.

Fig. 2 shows the changes made for PROMISE 2 to improve this situation. First, both end caps are made of insulating material in order to avoid short-circuiting of currents along the copper end cap at the bottom (those currents had been shown to be dangerous by possibly changing the rotation profile via azimuthal forces [13–15]). Second, both the upper and the lower end caps are split into two rings, the inner rotating with the inner cylinder and the outer rotating with the outer cylinder. In [16] it had been shown that this splitting yields a minimization of the Ekman pumping if the position of the splitting is at 0.4 of the gap width d. Third, the co-rotation of the two rings with one of the cylinders made it necessary to change the signal path of the ultrasonic transducers.

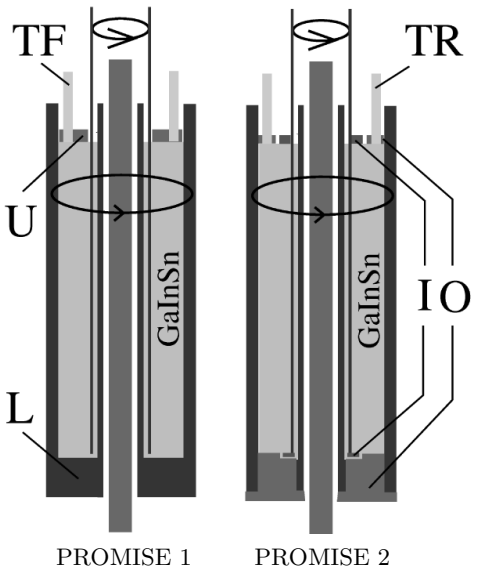

Fig. 2. The asymmetric end cap configuration in PROMISE 1 is replaced by a symmetric one in PROMISE 2. U – upper end cap fixed to the frame, L – lower copper end cap rotating with outer cylinder, I – inner rings, O – outer rings, TF – fixed ultrasonic transducer, TR – rotating ultrasonic transducer.

These two transducers provide full profiles of the axial velocity along the beam-lines parallel to the axis of rotation. While in PROMISE 1 they are inserted in the upper Plexiglass end cap that is fixed to the laboratory frame, in PROMISE 2 they must be connected via a sliding contact to the signal processing computer (DOP 2000).

The configuration of magnetic fields is the same for PROMISE 1 and PROMISE 2. An axial magnetic field of the order of 10 mT is produced by a double-layer coil with 76 windings (C in Fig. 1). The omission of windings at two symmetric positions close to mid-height, as seen in Fig. 1*a*, was motivated by a coil optimization to maximize the homogeneity of the axial field throughout the fluid volume. The coil is fed by currents up to 200 A, beyond which a significant heating of the coil sets in. The azimuthal field, also of the order of 10 mT, is generated by a current through a water-cooled copper rod R of radius 15 mm. The special power supply (PS in Fig. 1*c*) for this axial current is capable of delivering up to 8000 A.

3. Some results. We have carried out a large number of experimental runs in order to cover a wide range of parameter dependencies. Given the inner and outer radii of the TC cell, r_i and r_o (with a gap width $d = r_\mathrm{o} - r_\mathrm{i}$), the rotation rate of inner and outer cylinder, f_i and f_o, the axial magnetic field B_z and the azimuthal magnetic field at the inner cylinder, $B_\varphi(r_\mathrm{i})$, the governing dimensionless parameters are the Reynolds number $\mathrm{Re} := 2\pi f_\mathrm{i} d/\nu$, the ratio of rotation rates $\mu := f_\mathrm{o}/f_\mathrm{i}$, the Hartmann number $\mathrm{Ha} := B_z(r_\mathrm{i} d\sigma/\rho\nu)^{1/2}$, and the ratio of azimuthal to axial magnetic field $\beta := B_\varphi(r_\mathrm{i})/B_z$.

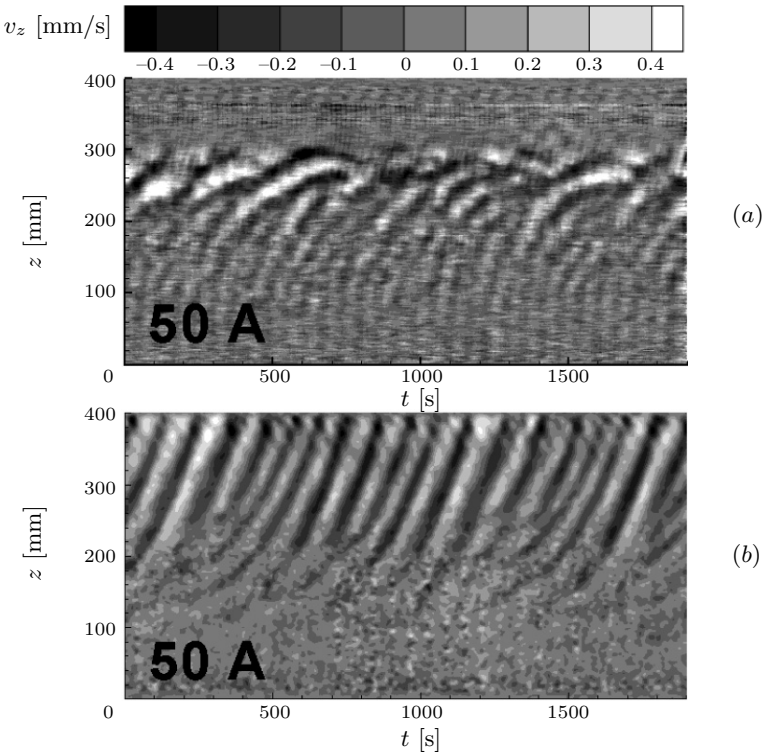

Fig. 3. Axial velocity perturbation for $f_\mathrm{i} = 0.06$ Hz (i.e., Re = 1779), $f_\mathrm{o} = 0.0162$ (i.e., $\mu = 0.27$), $I_\mathrm{coil} = 50$ A (i.e., Ha = 7.9). (*a*) PROMISE 1 with $I_\mathrm{rod} = 6000$ A (i.e., $\beta = 5.9$). (*b*) PROMISE 2 with $I_\mathrm{rod} = 7000$ A (i.e., $\beta = 6.9$).

Typically, the duration of an experimental run was 1900 sec, after a waiting time of one hour and more.

One of the most significant features of the MRI is that, for fixed Re and fixed azimuthal field B_ϕ, it shows up only in a finite interval of Ha [9]. This appearance and disappearance of a travelling mode is a suitable indicator for the existence of the proper MRI mode and its distinction from other possible flow structures.

In Fig. 3 we represent the results for rotation rates of $f_\mathrm{i} = 0.06\,\mathrm{Hz}$ (i.e., Re = 1779) and $f_\mathrm{o} = 0.0162$ (i.e., $\mu = 0.27$), which is slightly above the Rayleigh value $\mu_\mathrm{Ray} := r_\mathrm{i}^2/r_\mathrm{o}^2 = 0.25$. The current in the coil was fixed to $I_\mathrm{coil} = 50\,\mathrm{A}$ (i.e., Ha = 7.9). In the PROMISE 1 case (Fig. 3*a*), the axial current was set to $I_\mathrm{rod} = 6000\,\mathrm{A}$ (i.e., $\beta = 5.9$), in the PROMISE 2 (Fig. 3*b*) case to $I_\mathrm{rod} = 7000\,\mathrm{A}$ (i.e., $\beta = 6.9$), a difference that is, however, not essential. The grey scale of the plots indicates the axial velocity component v_z measured along the ultrasound beam, from which we have subtracted the (z-dependent) time average in order to filter out the two Ekman vortices, which appear already without any magnetic field. These Ekman vortices, which in the PROMISE 1 version are characterized by inward radial flows close to the upper and lower end-plates and a jet-like radial outflow in the centre of the cylinder [17], are significantly suppressed in the PROMISE 2 version due to the use of split end caps. In PROMISE 1, the wave dies away at the position of the radial jet (which is not always at mid-height). In contrast to this, in PROMISE 2 the wave propagates throughout the total height of the cell. More details about the reduction of the Ekman pumping in PROMISE 2, and about the consequences for the propagation of the MRI wave will be published elsewhere [18].

This much improved behaviour of the MRI in PROMISE 2 can be visualized nicely when crossing the Rayleigh line. The importance of this line, which, together with the Velikhov–Chandrasekhar line, bounds the region of MRI, is illustrated in Fig. 4. It is known [11] that, for applied helical fields, the travelling wave appears already with a stationary outer cylinder, i.e., at $\mu = 0$, although with a very low frequency. With increasing μ, the wave frequency increases and typically reaches a value of $(0.1....0.2)f_\mathrm{i}$ at the Rayleigh value $\mu_\mathrm{Ray} = 0.25$. Fig. 5 now shows in

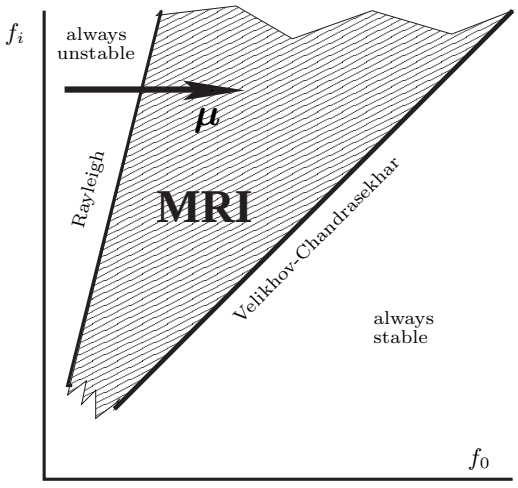

Fig. 4. Stability diagram of a TC flow with and without magnetic fields. Whereas the hydrodynamic Rayleigh line separates flows with increasing and decreasing angular momentum, the magnetohydrodynamic Velikhov-Chandrasekhar line separates flows with increasing and decreasing angular velocity.

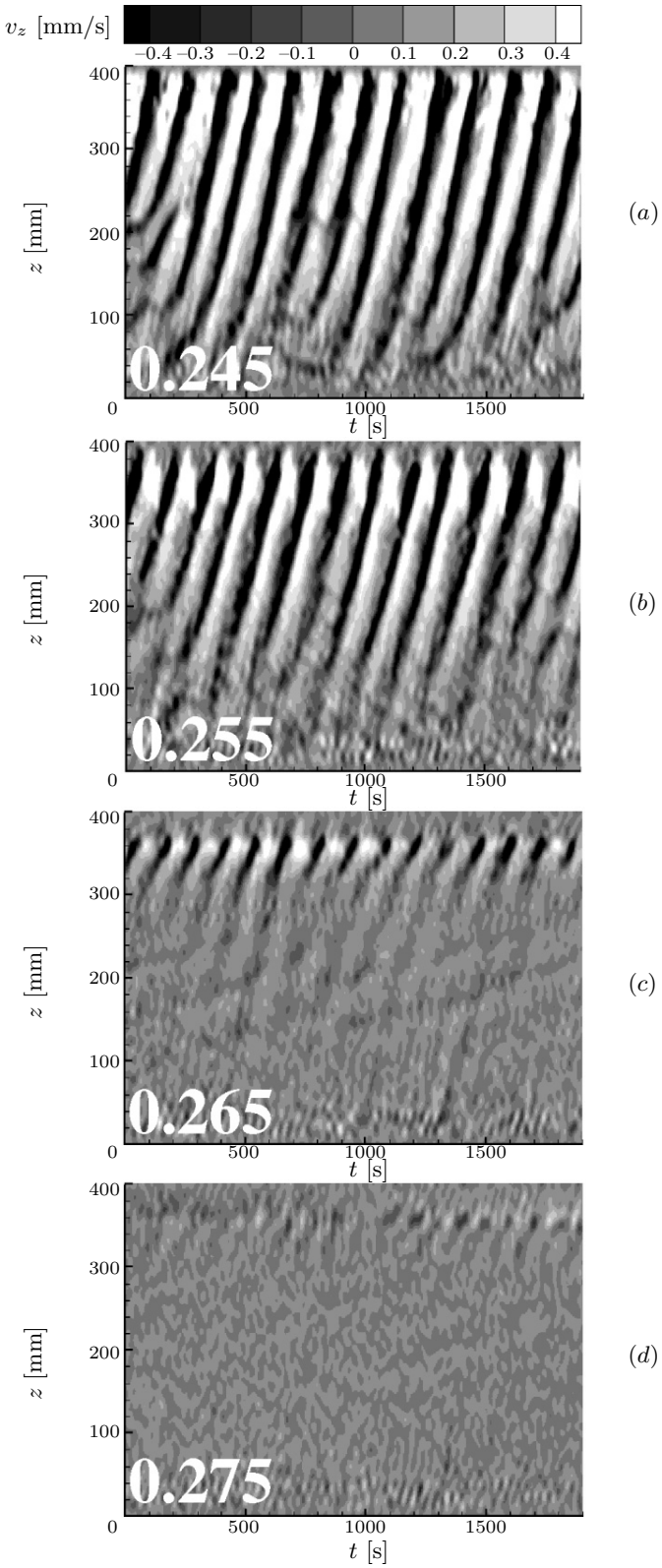

Fig. 5. Measured axial velocity perturbations for μ =0.245, 0.255, 0.265, and 0.275, at $f_{\rm i} = 0.1\,{\rm Hz}$, $I_{\rm coil} = 76\,{\rm A}$, $I_{\rm rod} = 4000\,{\rm A}$.

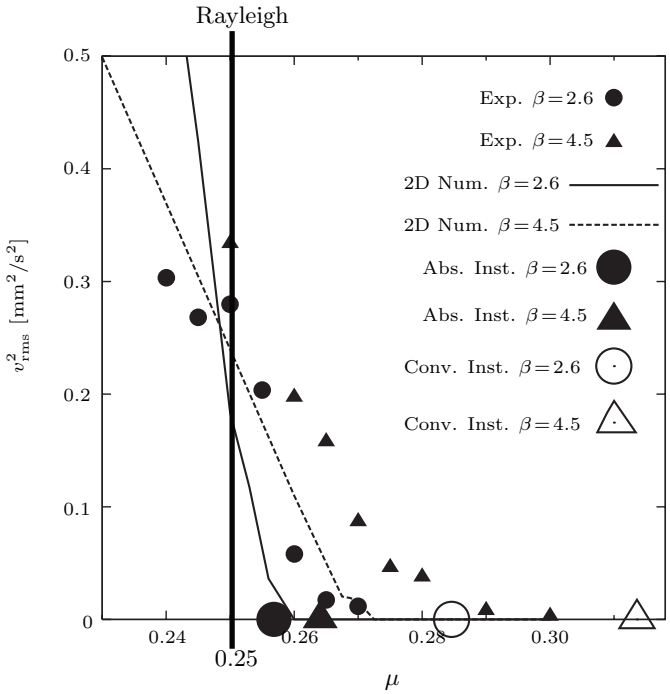

Fig. 6. Rms of the velocity perturbation for $f_{\rm i} = 0.1\,{\rm Hz}$, $I_{\rm coil} = 76\,{\rm A}$, and two values of $I_{\rm rod} = 4000\,{\rm A}$ and $7000\,{\rm A}$, which correspond to $\beta = 2.6$ and $\beta = 4.5$, respectively. The experimental values (small circles and triangles) are compared with the numerical results of a 2D solver and with the results for the absolute and the convective instability of a 1D eigenvalue solver (courtesy of Jānis Priede).

detail what happens with the travelling MRI wave when μ crosses the Rayleigh line. The parameters for this run were $f_{\rm i} = 0.1\,{\rm Hz}$ (i.e., ${\rm Re} = 2958$), $I_{\rm coil} = 76\,{\rm A}$ (i.e., ${\rm Ha} = 12$), $I_{\rm rod} = 4000\,{\rm A}$ (i.e., $\beta = 2.59$). It is clearly visible that the MRI wave is still present at $\mu = 0.255$, becomes significantly weaker at $\mu = 0.265$, and has completely died at $\mu = 0.275$.

This transition is further analyzed in Fig. 6, which shows the rms of the axial velocity perturbationin dependence on μ, now both for $I_{\rm rod} = 4000\,{\rm A}$ and $I_{\rm rod} = 7000\,{\rm A}$ (which corresponds to $\beta = 2.6$ and 4.5, respectively).

The measured values (full lines) are compared with the numerical results of a 2D solver (dashed lines), but also with the results of a 1D solver for the onset of the absolute and the convective instability [19, 20] (courtesy of Jānis Priede). It is most remarkable that the 1D results for the onset of the absolute instability correspond nearly perfectly to the results of the 2D solver, while the thresholds for the convective instability are situated at much higher values of μ. Compared to the 2D numerical curves, the experimental curves are shifted only slightly towards higher μ. As expected, we see also that for increasing β the threshold of the instability shifts to higher values of μ.

4. Conclusions. We have obtained experimental evidence for the existence of the MRI in current-free helical magnetic fields. The symmetrization of the axial boundary conditions and the use of split end caps in PROMISE 2 has led to a strong reduction of the Ekman pumping and, hence, to an avoidance of artefacts in the radial jet flow region. The MRI wave extends clearly beyond the Rayleigh

line, and its behaviour is in good correspondence with both 2D simulations and 1D simulations for the absolute instability, but in stark contrast with 1D simulations for the convective instability. This indicates that the observed MRI wave is indeed a global instability and not only a noise-triggered convective instability as claimed recently [21]. Further dependencies of the MRI on parameters like Re, β, and Ha, as well as their comparison with numerical predictions will be published elsewhere [18].

Acknowledgements. We are grateful to Jānis Priede for many fruitful discussions on MRI and for sharing with us his results for the convective and absolute instability. This work was supported by the German Leibniz Gemeinschaft within its "Senatsausschuss Wettbewerb" (SAW) programme and by Deutsche Forschungsgemeinschaft in the frame of SFB 609.

REFERENCES

[1] E.P. Velikhov. Stability of an ideally conducting liquid fluid between cylinders rotating in a magnetic field. *Sov. Phys. JETP*, vol. 9 (1959), pp. 995–998.

[2] S.A. Balbus and J.F. Hawley. A powerful local shear instability in weakly magnetized disks. 1. Linear analysis. *Astrophys. J.*, vol. 376 (1991), pp. 214–222.

[3] A. Gailitis, O. Lielausis, E. Platacis, G. Gerbeth, and F. Stefani. Colloquium: Laboratory experiments on hydromagnetic dynamos. *Rev. Mod. Phys.*, vol. 74 (2002), pp. 973–990.

[4] F. Stefani, A. Gailitis, and G. Gerbeth. Magnetohydrodynamic experiments on cosmic magnetic fields. *ZAMM*, 88 (2008), 930–954.

[5] D. Sisan *et al.* . Experimental observation and characterization of the magnetorotational instability. *Phys. Rev. Lett.*, vol. 93 (2004), Art. No. 114502.

[6] H.T. Ji, M. Burin, E. Schartman, and J. Goodman. Hydrodynamic turbulence cannot transport angular momentum effectively in astrophysical disks. *Nature*, vol. 444 (2006), pp. 343–346.

[7] E. Schartman, H. JI, and M. Burin. Development of a Couette-Taylor flow device with active minimization of secondary circulation. *Rev. Sci. Instr.*, vol. 80 (2009), Art. No. 024501.

[8] R. Hollerbach and G. Rüdiger. New type of magnetorotational instability in cylindrical Taylor–Couette flow. *Phys. Rev. Lett.*, vol. 95 (2005), Art. No. 124501.

[9] F. Stefani *et al.* . Experimental evidence for magnetorotational instability in a Taylor-Couette flow under the influence of a helical magnetic field. *Phys. Rev. Lett.*, vol. 97 (2006), Art. No. 184502.

[10] G. Rüdiger *et al.* . The travelling-wave MRI in cylindrical Taylor–Couette flow: Comparing wavelengths and speeds in theory and experiment. *Astrophys. J.*, vol. 649 (2006), pp. L145–L147.

[11] F. Stefani *et al.* . Experiments on the magnetorotational instability in helical magnetic fields. *New J. Phys.*, vol. 9 (2007), Art. No. 295.

[12] F. Stefani *et al.* . Results of a modified PROMISE experiment. *Astron. Nachr.*, vol. 329 (2008), pp. 652–658.

[13] J. Szklarski. Ekman-Hartmann layer in a magnetohydrodynamic Taylor–Couette flow. *Phys. Rev. E*, vol. 76 (2007), Art. No. 066308.

[14] J. Szklarski and G. Gerbeth. Boundary layer in the MRI experiment PROMISE. *Astron. Nachr.*, vol. 329 (2008), pp. 667–674.

[15] J. Priede. Pseudo-magnetorotational instability in a Taylor–Dean flow between electrically connected cylinders. *Phys. Rev. E*, vol. 79 (2009), Art. No. 066314.

[16] J. Szklarski. Reduction of boundary effects in spiral MRI experiment PROMISE. *Astron. Nachr.*, vol. 328 (2007), pp. 499–506.

[17] A. Kageyama, H. Ji, J. Goodman, F. Chen, E. Shoshan. Numerical and experimental investigation of circulation in short cylinders. *J. Phys. Soc. Jpn.*, vol. 73 (2004), pp. 2424–2437.

[18] F. Stefani *et al.* . Helical magnetorotational instability in a Taylor–Couette flow with strongly reduced Ekman pumping. Phys. Rev. E, submitted (2009): arXiv: 0904.1027.

[19] J. Priede, I. Grants, and G. Gerbeth. Inductionless magnetorotational instability in a Taylor–Couette flow with a helical magnetic field. *Phys. Rev. E*, vol. 75 (2007), Art. No. 047303.

[20] J. Priede and G. Gerbeth. Absolute versus convective helical magnetorotational instability in a Taylor–Couette flow. *Phys. Rev. E*, vol. 79 (2009), Art. No. 046310.

[21] W. Liu. Noise-sustained convective instability in a magnetized Taylor–Couette flow. *Astrophys. J.*, vol. 692 (2009), pp. 698–1003.

Received 21.05.2009